First-Principle Calculations of Pressure-Induced Changes in Structural, Electronic, and Optical Properties of $CuMX_2$ (M = Ga, In; X = S, Se, Te) Chalcopyrites

V. Jayalakshmi[#,*] and G. Jaiganesh[@]

[#]Department of Physics, SRM Institute of Science and Technology, Ramapuram Campus, Chennai – 600089.

[@]Materials Science Group, Indira Gandhi Centre for Atomic Research, Kalpakkam – 603102.

*Corresponding authorsEmail: jayam6480@gmail.com

Abstract

In this study, we investigate the electronic structure, structural phase stability, and optical properties of $CuMX_2$ chalcopyrite semiconductors (M = Ga, In; X = S, Se, Te) using the self-consistent linear muffin-tin orbital method (LMTO) within the local density approximation (LDA). The total energies and equilibrium lattice constants are computed as a function of reduced volume using the tight-binding version of LMTO (TB-LMTO). The chalcopyrites undergo a structural phase transition from BCT (Chalcopyrite) to face-centered cubic phase (FCC) under high pressure, with the BCT phase being more energetically stable than the intermediate distorted simple cubic phase (d-SC). Band structures are analyzed for both equilibrium and high-pressure phases, revealing metallic behavior in the high-pressure FCC phase. Optical properties are studied using the full potential version of the linear muffin-tin orbital method (FP-LMTO) within LDA, and the complex dielectric functions and refractive indices 'n' are presented.

Keywords: Electronic Structure, Structural Phase Transition, Optical Properties, High-Pressure studies.

1. Introduction

Chalcopyrite semiconductors from the I-III-VI_2 family have gained significant attention for their diverse technological applications [1].These compounds share isoelectronic characteristics with Zinc-blend (ZB)-type II-VI semiconductor compounds [2]. With a direct bandgap and tetragonal chalcopyrite crystal structure, the ternary compounds studied here are crucial for various fields, including non-linear optics, optoelectronics, and photovoltaic devices [3-9].

However, due to their structural complexity, electronic structure calculations for chalcopyrite unit cells are more intricate than those for binary ZB-type semiconductors. The cation distribution in the chalcopyrite structure (body-centered tetragonal–BCT) differs from ZnS, resulting in a tetragonal unit cell with the c-axis approximately twice the a-axis of the ZB-type unit cell. Under pressure, these compounds undergo a phase transition from an open tetrahedral structure to a closely packed cubic structure with an octahedral arrangement [10]. This pressure-induced transition is also observed in the IV-III-V and II-IV families [10]. As a consequence, high-pressure phase transitions in these compounds have garnered considerable attention, leading to significant changes in bonding, structure, and associated properties [10].

Werner et al. [10] observed a pressure-induced phase transformation from chalcopyrite to NaCl phase in CuGaS2 at around 16 GPa. T. Tinoco et al. [11] reported a phase change from BCT to cubic phase in $CuInS_2$ and $CuInSe_2$ with a volume reduction of approximately 10%. Gonzalez et al. [12] measured optical absorption in a diamond anvil cell and found an irreversible phase transition to NaCl structure. M. I. Alonso et al. [13] calculated complex dielectric components for $CuMX_2$ (M = Ga, In; X = S, Se) chalcopyrites using spectroscopic ellipsometry. Y. Mori et al. [14] observed the possibility of a distorted simple cubic (d-SC) phase between BCT and high-pressure FCC phase in $CuGaTe_2$ and $CuInTe_2$.

Jaffe et al. [15-16] used the self-consistent potential-variation mixed basis (PVMB) approach to study ambient pressure ternary chalcopyrite semiconductors' band structure, electronic charge densities, density of states, and chemical bonding. Jaffe et al. [17] employed the first principle and self-consistent mixed-based potential-variation (MBPV) band structure method to observe valence-band X-ray photoemission spectra for CuInSe2 frozen Cu 3d orbitals. Other theoretical work based on the self-consistent approach has been reported [18-21],

including the electronic and optical properties of the BCT phase of Cu-based chalcopyrite semiconductors [19].

The present study utilizes the self-consistent Tight Binding version of the LMTO (TB-LMTO) method [22-24] to investigate the structural phase stability and high-pressure behavior of $CuMX_2$ (M = Ga, In; X = S, Se, Te) chalcopyrite compounds. Phase transformations from BCT to FCC under pressure are examined, and energetically favored c/a and u values for the compounds are estimated at ambient conditions. Lattice constants are computed using the calculated c/a ratio and u values, and the energy band gaps for the BCT phase are determined from the electronic band structure.

Optical properties of $CuMX_2$ (M = Ga, In; X = S, Se, Te) chalcopyrites are obtained using the full potential version (FP-LMTO) 'LmtART' method [25]. Dielectric complex functions $\varepsilon1(\omega)$ and $\varepsilon2(\omega)$ are calculated, and refractive indices are derived from the real and imaginary parts of the dielectric function. The degree of anisotropy is determined using the static dielectric functions.

In this study, we employed the numerical atomic orbital (NAO) pseudopotential method with a localized basis set to calculate dielectric functions, refractive indices, and optical absorption coefficients for $CuMX_2$ ternary chalcopyrites. The calculation method, results, discussions, and conclusions are presented in the following sections.

2. Method of calculation

In this study, we employ the TB-LMTO method to calculate the total energies and their variations with volume for $CuMX_2$chalcopyrites in ambient and high-pressure phases. The calculations are performed within the Local Density Approximation, considering the exchange-correlation potential based on the von Barth and Hedin formalism [26]. We account for the relativistic mass-velocity variation but neglect spin-orbit coupling. Valence states are treated for Cu, Ga, In, S, Se, and Te atoms. The BCT phase (I4_2d) is considered for ambient conditions, while under high pressure, a phase transition to the FCC phase (Fm3m) occurs. Eigenvalues are calculated with self-consistent accuracy, using appropriate k-point convergence for each phase. The Birch Murnaghan equation of state is employed to estimate the total energies and derive the pressure-volume relation and bulk modulus (B_0). The density of states and bandgap (E_g) are also computed and compared with available data.

For the full potential LMTO calculations of optical properties, we use the 'LmtART' program within LDA. The PLW approximation is employed, representing the potential with non-overlapping muffin-tin spheres and expanding the interstitial region using plane waves. Spin-orbit coupling is neglected. The dielectric function ε(ω), refractive index 'n', and degree of anisotropy are calculated using a Fourier-transformed wave function and potential in the interstitial region with a 42×42×42 mesh.

3. Results and Discussion

In this study, we extensively investigate the variations in total energy with volume for $CuMX_2$chalcopyrites using the TB-LMTO method. Firstly, we calculate the energetically favorable 'c/a' ratio and 'u' value for S, Se, and Te at ambient conditions for the mentioned $CuMX_2$ compounds. The optimization of the 'u' value is done based on experimental data, while the 'c/a' ratio is optimized using available experimental values. With the optimized 'c/a' and 'u' parameters, we calculate the equilibrium lattice parameter for each compound. The total energy values are then obtained and fitted using the Birch-Murnaghan equation of state. In Table 1, we present the calculated lattice parameters and bulk moduli for the BCT and FCC phases of all compounds, alongside available experimental and previously reported values for comparison.

Subsequently, we explore the structural phase transitions of $CuMX_2$ compounds. At ambient conditions, these compounds crystallize in the BCT phase and remain stable. The atomic positions for the BCT phase are given as follows: Cu at (0, 0, 0), M at (0, 0, 0.5), and X at (u, 0.25, 0.125). The calculated 'u' and 'c/a' values for BCT-type CuGaS2 are 0.256 and 1.9574, respectively. Figure (1a) illustrates the crystal structure of the BCT phase. However, under high pressure, these compounds undergo a structural phase transition from BCT to FCC phase. The atomic positions for the FCC phase are Cu at (0, 0, 0), M at (0.5, 0.5, 0.5), and X at (0.25, 0.25, 0.25). The crystal structure of the high-pressure FCC phase is depicted in Figure (1b). Total energy values are calculated while varying the relative volume from 1.2 V/V0 to 0.5 V/V0 in steps of 0.5 V/V0, where V0 is the experimental volume. The calculated total energy values are then fitted using the Birch-Murnaghan equation of state. The resulting total energy versus relative volume graph for each compound is presented in the figures.

In our study, we comprehensively investigate the electronic structure and structural phase stability of all $CuMX_2$chalcopyrites. The calculated 'u' values are determined as 0.253 for

$CuGaSe_2$, 0.26 for $CuGaTe_2$, 0.23 for $CuInS_2$, 0.236 for $CuInSe_2$, and 0.225 for $CuInTe_2$. These values are in excellent agreement with experimental [17] and reported values [18]. Additionally, we theoretically calculate the 'c/a' values as 2.020 for $CuGaSe_2$, 1.990 for $CuGaTe_2$, 1.999 for $CuInS_2$, 2.0098 for $CuInSe_2$, and 2.0043 for $CuInTe_2$. Under pressure, $CuGaSe_2$, $CuInS_2$, and $CuInSe_2$chalcopyrites undergo a phase transition from the stable BCT phase to the FCC phase. However, for $CuMTe_2$, it has been experimentally reported [14] that an intermediate distorted simple cubic phase (d–SC) exists between the stable BCT and FCC phases. In our calculation, we consider the d–SC phase to check the phase stability of $CuMTe_2$ compounds. However, our findings reveal that the BCT phase is energetically more favorable than d–SC, raising the need for detailed experimental investigations of these two compounds. Therefore, for the total energy calculation, we only consider the d–SC phase to assess the compounds' phase stability. In the case of the FCC phase, the positions are taken as the same as those for the $CuGaS_2$ compound. The total energy values are then calculated by varying the relative volume and fitted using the Birch-Murnaghan equation of state. The obtained fitted values are used to plot the total energy versus relative volume graphs, enabling the calculation of the volume of transition for the compounds.

Figures 2 to 7 illustrate the variation of total energy with respect to the relative volume for $CuMX_2$ compounds. From the graphs, the volume of transition is determined as 0.74 V/V0 for $CuGaS_2$ and 0.775 V/V0 for $CuGaSe_2$, 0.8 V/V0 for $CuGaTe_2$, 0.74 V/V0 for $CuInS_2$, 0.71 V/V0 for $CuInSe_2$, and 0.75 V/V0 for $CuInTe_2$. The calculated lattice constants and bulk moduli for the BCT phase of $CuMX_2$ are presented in Table 1, alongside available experimental [26,27] and reported values [17,18,20,11]. The lattice constants agree well with available experimental and other theoretical values. The cell volume and bulk modulus for the FCC phase of the compounds are shown in Table 2, which requires experimental data for comparison. It is observed that the lattice parameter increases and the bulk modulus decreases from S to Te, with $CuMTe_2$ (M = Ga, In) being more easily compressible than the other compounds.

During the transition from BCT to FCC phases, the enthalpies of both phases become equal. To analyze this transition, we calculate the Equation of State (EOS) using the fitted total energy values. Figures 8 to 10 present the EOS graphs for $CuMX_2$ (M = Ga, Te; X = S, Se, Te) compounds. The critical pressure at which the structural transition occurs is found to be 28.368 GPa for $CuGaS_2$, 24.68 GPa for $CuInS_2$, 18.977 GPa for $CuGaSe_2$, 22.42 GPa for $CuInSe_2$, 6.714

GPa for $CuGaTe_2$, and 9.913 GPa for $CuInTe_2$. Additionally, from the EOS graphs, we calculate the volume collapse, which is approximately 17.5% for $CuGaX_2$ compounds, 15% for $CuInS_2$ and $CuInTe_2$, and 12.5% for $CuInSe_2$.

Next, we investigate the band structure of $CuMX_2$ in both the BCT and FCC phases. Figures 11 and 12 illustrate the band structure profiles for the BCT phase of $CuGaX_2$ and $CuInX_2$ compounds. The calculated band structures for $CuMX_2$ in the BCT structure follow the symmetry direction T-Γ-N. At the ambient BCT phase, the band structure displays a direct bandgap, where the valence band maximum and conduction band minimum meet at the Γ point. The presence of noble metal d-levels significantly influences the uppermost valence bands of the I-II-VI2 compound in the valence band. On the other hand, Figures 13 and 14 show the band structure for the FCC phase of $CuGaX_2$ and $CuInX_2$ compounds, demonstrating metallization under high pressure as the profiles cross the Fermi level. Our band structure calculations for these chalcopyrites confirm the transition of the compounds from semiconductor to metal under high pressure.

Moreover, we analyze the density of states for both the BCT and FCC phases using the tetrahedron method. The bandgap values are underestimated due to LDA, resulting in 1.0 eV, 0.75 eV, and 0.81 eV bandgap values for the $CuGaX_2$ (X = S, Se, Te) compounds, and 0.5 eV, 0.375 eV, and 0.5 eV bandgap values for $CuInX_2$ compounds. The electronic structure of the upper valence band is dominated by Cu-d and X-p interactions, distinguishing it from binary semiconductors. Table 3 presents the calculated 5f bandgap values for $CuMX_2$, which are compared with available experimental and theoretical values [16, 20].

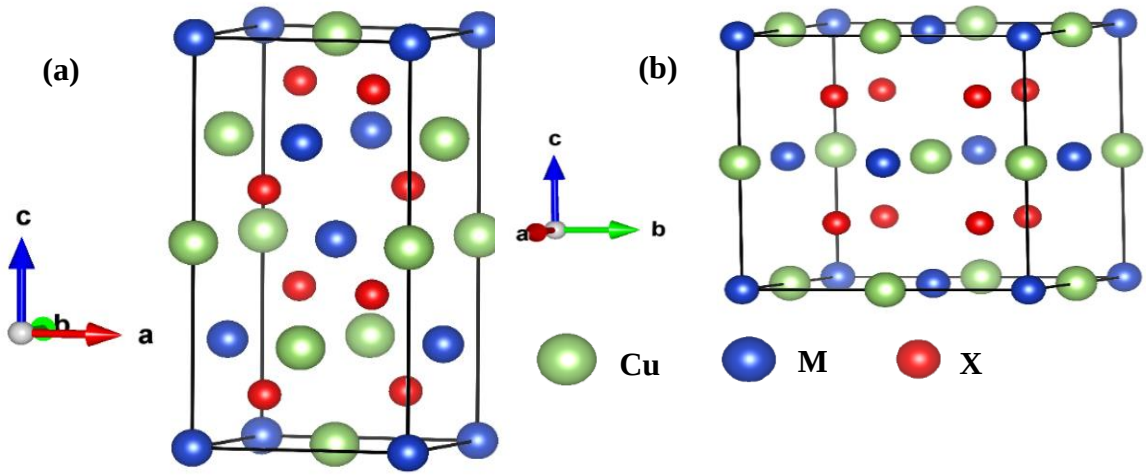

Fig:1(a) and 1(b) represents the crystal structure of BCT and FCC phase of ternary chalcopyrite

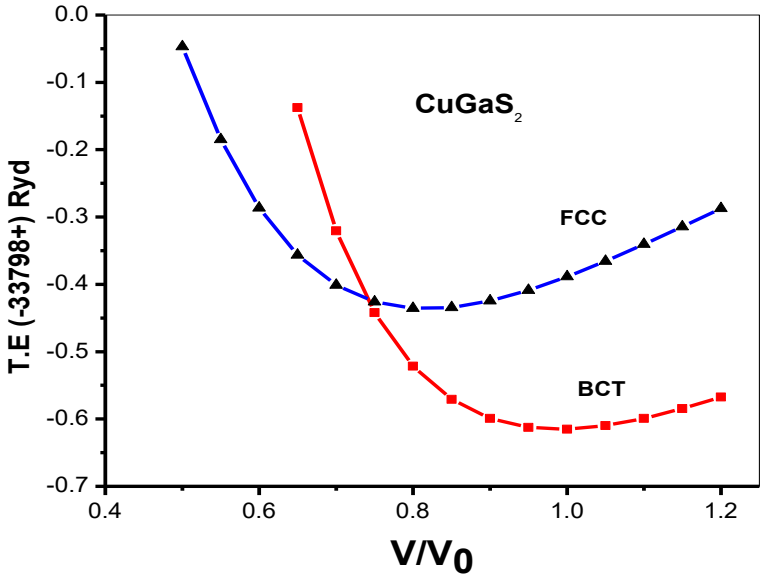

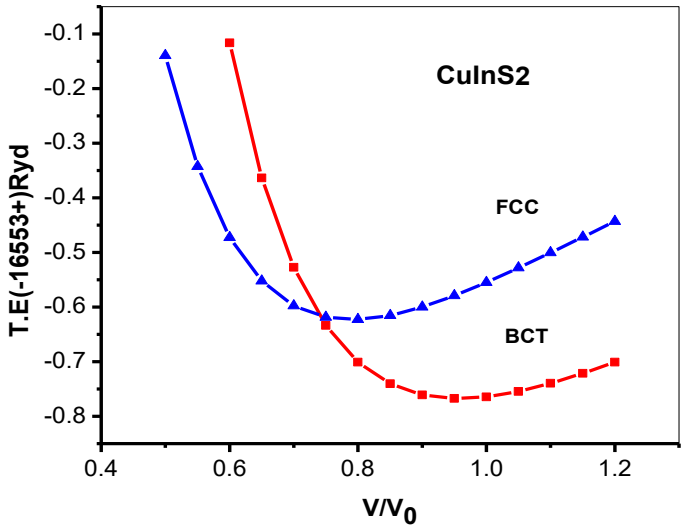

Fig: 2 & 3. The computed total energy versus relative volume of $CuGaS_2$ and $CuInS_2$

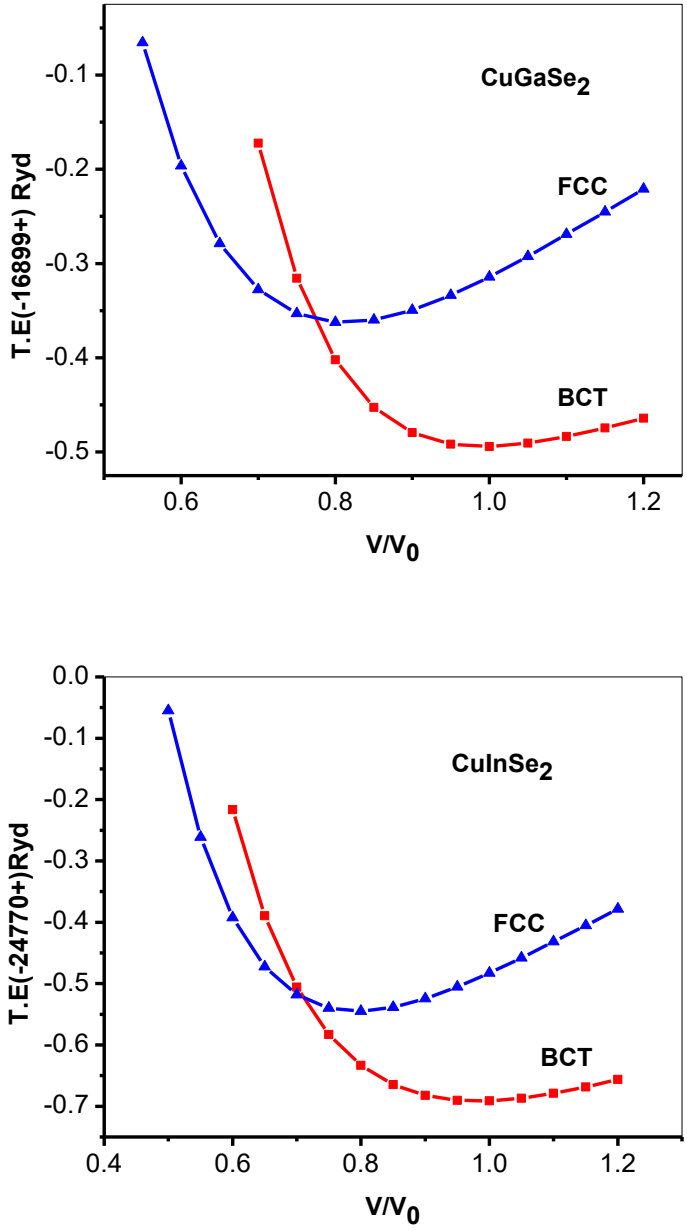

Fig: 4&5. The computed total energy versus relative volume of $CuGaSe_2$ and $CuInSe_2$

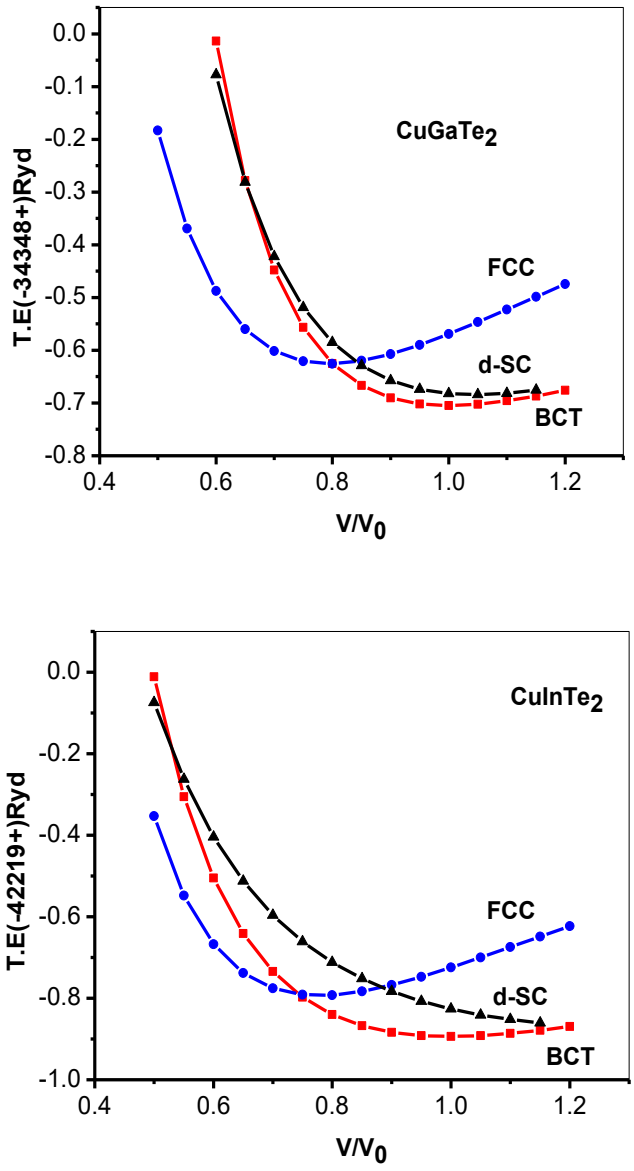

Fig: 6 &7. The computed total energy versus relative volume of $CuGaTe_2$ and $CuInTe_2$

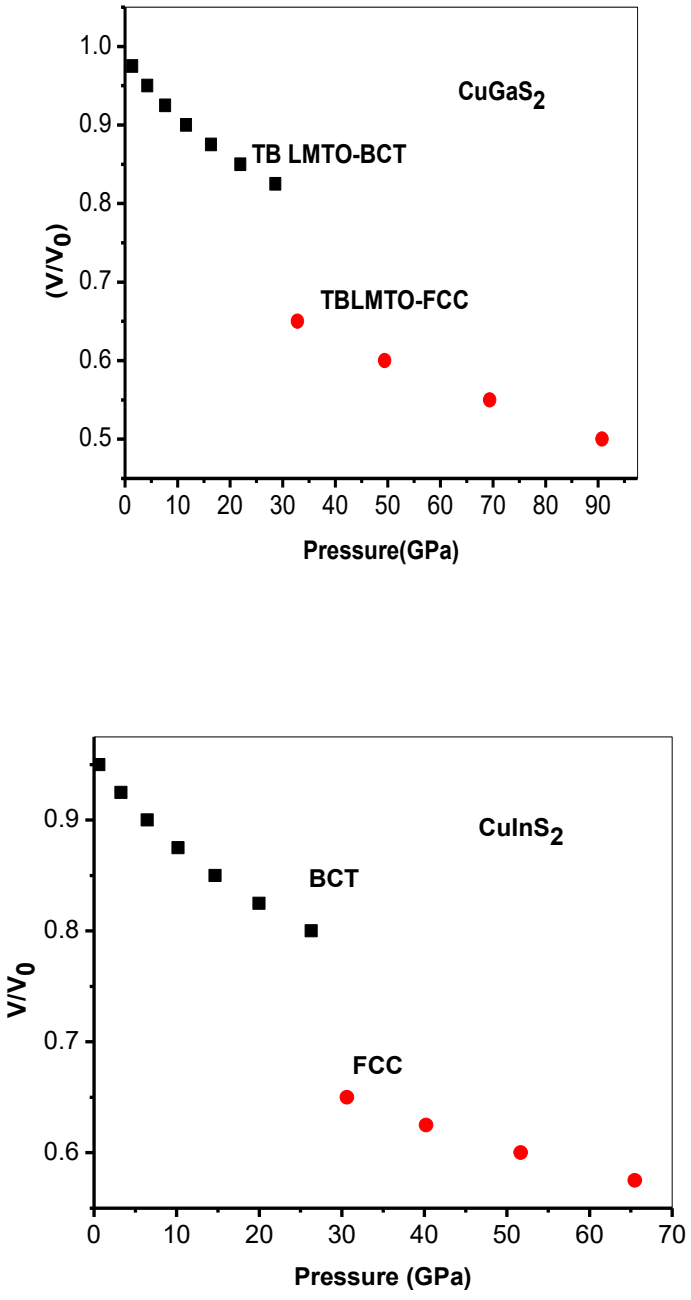

Fig: 8. Pressure-Volume data of $CuGaS_2$ and $CuInS_2$

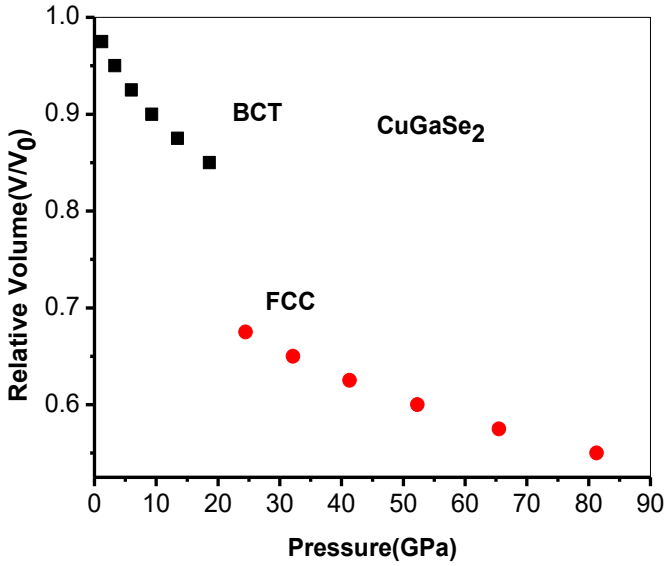

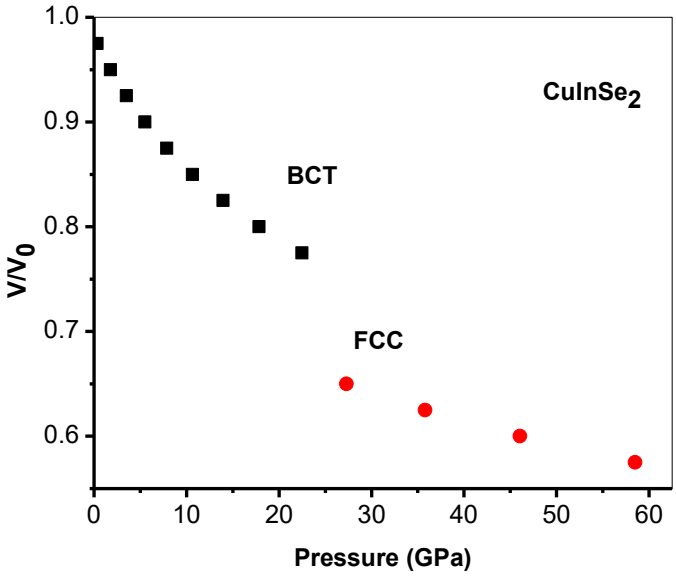

Fig: 9. Pressure-Volume data of $CuGaSe_2$ and $CuInSe_2$

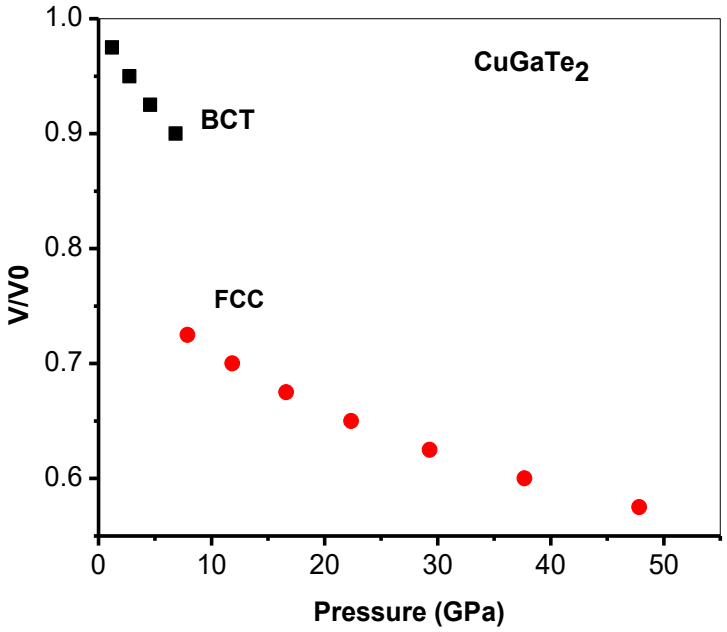

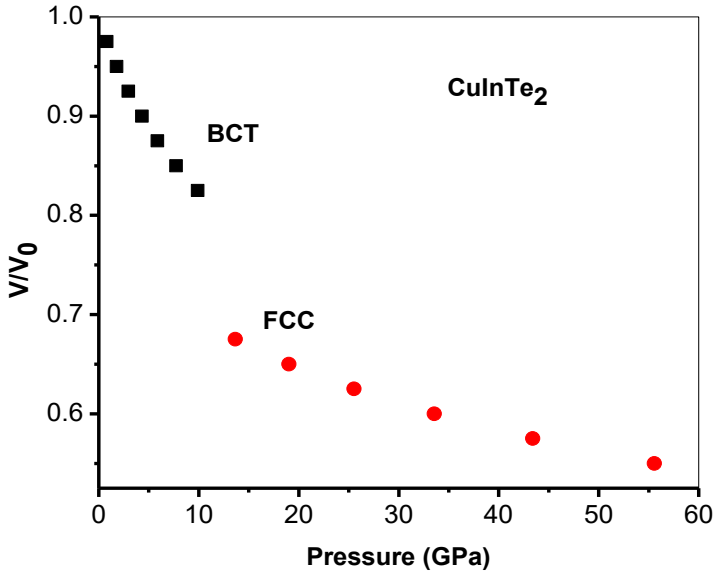

Fig: 10. Pressure-Volume data of $CuGaTe_2$ and $CuInTe_2$

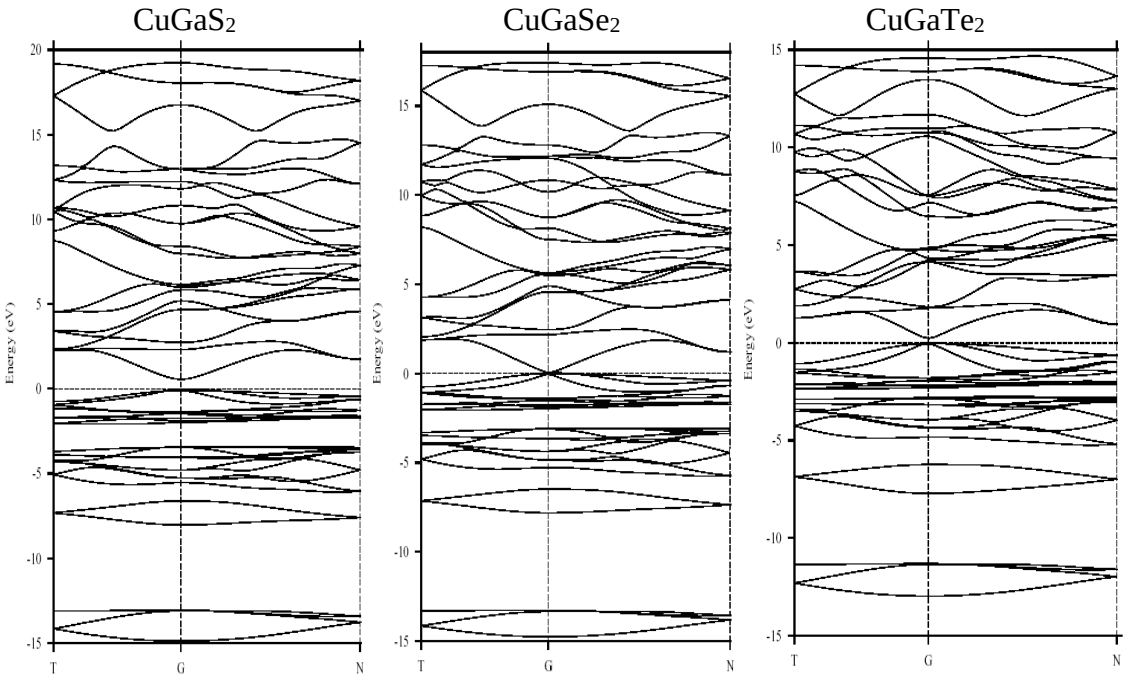

Fig: 11. The band structure profile for the BCT phase of $CuGaS_2$, $CuGaSe_2$, and $CuGaTe_2$.

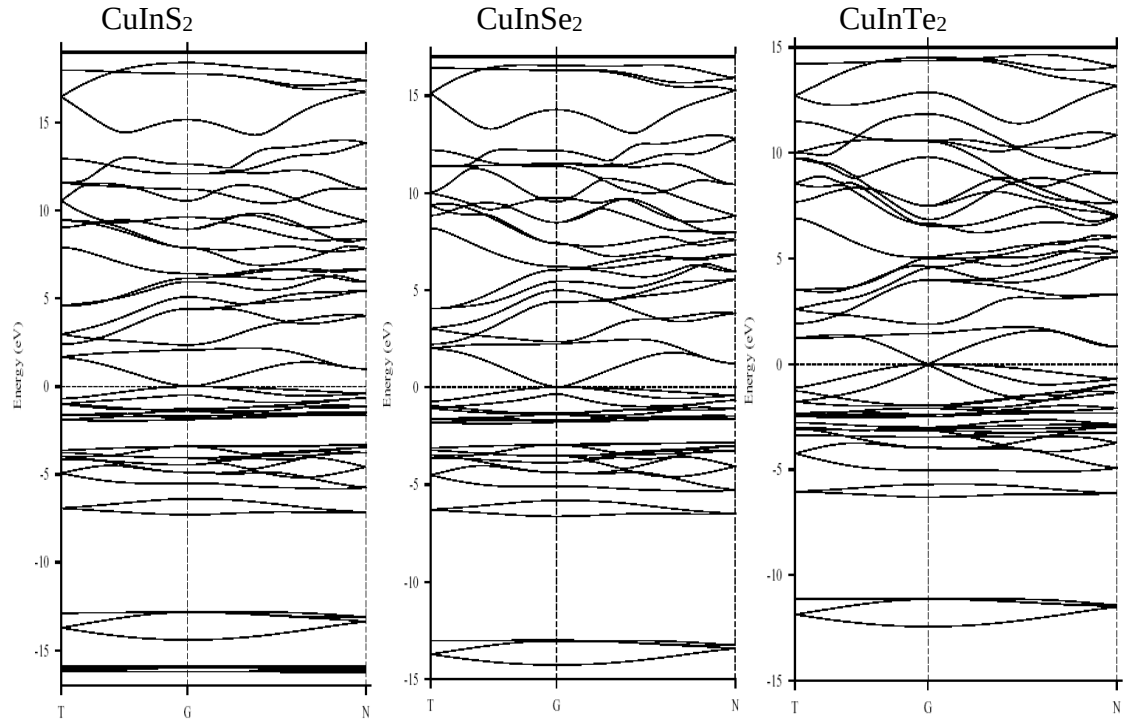

Fig: 12. The band structure profile for the BCT phase of $CuInS_2$, $CuInSe_2$, and $CuInTe_2$.

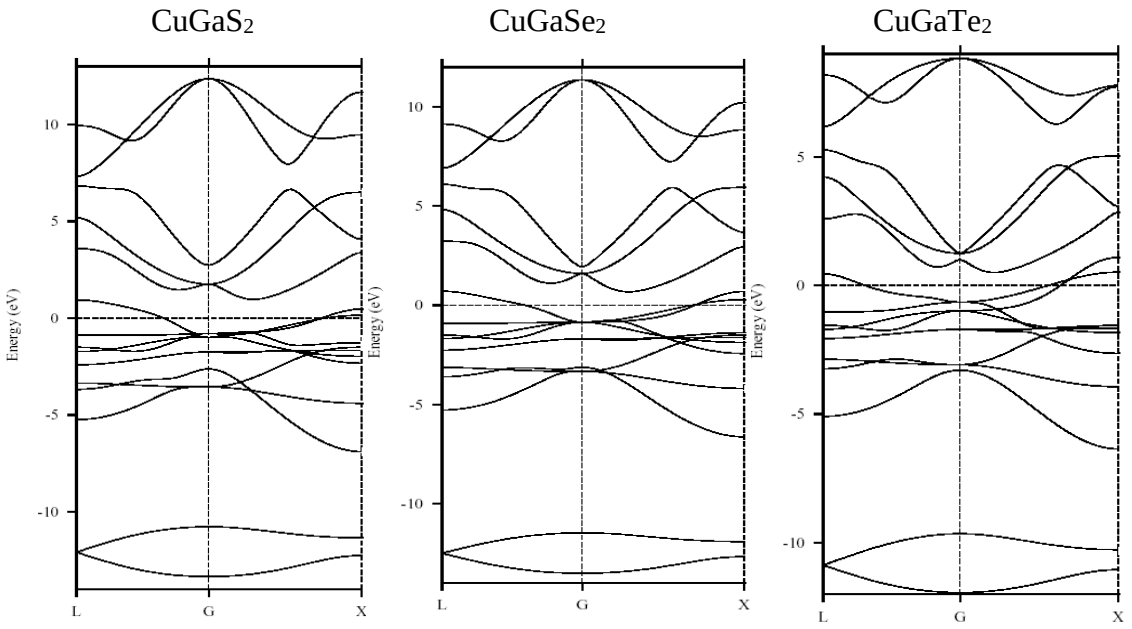

Fig: 13. The band structure profile for the FCC phase of $CuGaS_2$, $CuGaSe_2$, and $CuGaTe_2$.

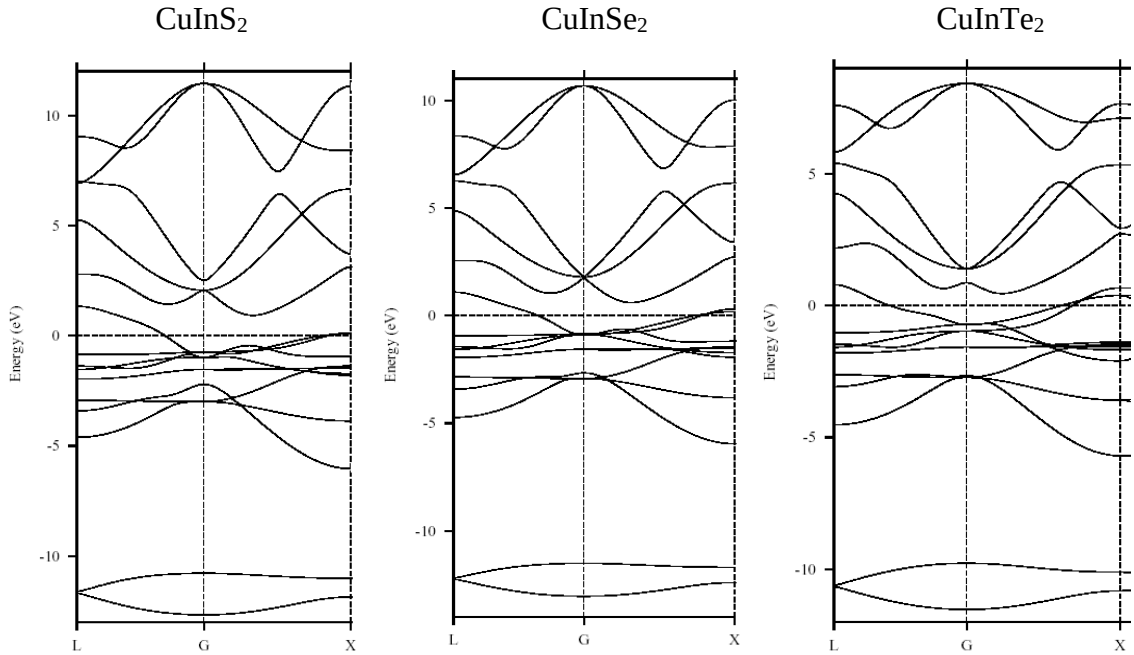

Fig: 14 The band structure profile for the FCC phase of $CuInS_2$, $CuInSe_2$ and $CuInTe_2$.

Table: 1. Calculated lattice parameters and bulk modulus for BCT-type $CuMX_2$compounds with the available experimental and earlier reported data.

	a (Å)	c (Å)	Bulk modulus (GPa)	B'	*'u'*value
$CuGaS_2$	5.32 (5.349 [a], 5.347[b])	10.58 (10.47[a], 10.974[b])	94.65 (98.02[b], 95.8[d])	3.06	0.256 (0.25[a], 0.251[b])
$CuGaSe_2$	5.55 (5.607[a], 5.607[b])	11.21 (10.99[a], 10.99 [b])	63.34 (69.31[b], 76.6[d])	4.1	0.253 (0.25[a], 0.252[b],)
$CuGaTe_2$	5.99 (5.994[a], 5.994[b])	11.92 (11.91[a], 11.912[b])	46.30 (55.4[e], 48.50[b])	2.57	0.260 (0.25 [a], 0.25 [b])
$CuInS_2$	5.47 (5.517[a], 5.561[c])	10.93 (11.06[a], 11.116[c])	89.56 (75±5[c], 71.1[d])	1.2	0.230 (0.20[a], 0.229[b])
$CuInSe_2$	5.78 (5.773[a], 5.797[c])	11.62 (11.55[a], 11.585[c])	50.06 (72±2[c],53.6 [d])	4.5	0.236 (0.22 [a])
$CuInTe_2$	6.19 (6.167[a], 6.179[b])	12.42 (12.34[a], 12.36 [b])	31.80 (45[b], 36.0[d])	1.37	0.225 (0.225[a], 0.225[b])

[a]ref [17], [b]ref[18],[c]ref [11], [d]experemientalvalue ref [27,28].

Table: 2.Calculated cell volume and bulk modulus for $CuMX_2$ compounds in the high-pressure FCC phase

	Cell Volume (a.u.)	Bulk Modulus (GPa)
$CuGaS_2$	412.89	96.00
$CuGaSe_2$	473.47	85.17
$CuGaTe_2$	573.81	68.58
$CuInS_2$	458.40	99.09
$CuInSe_2$	520.47	83.72
$CuInTe_2$	625.48	66.83

Table: 3. Calculated bandgapsfor $CuMX_2$ compounds with the available experimental and reported values

	The bandgap (eV)	
	Present Values	Exp/Reported values
$CuGaS_2$	1.0	2.43 [a], 0.903[e] 1.25 [c]
$CuGaSe_2$	0.75	1.68 [a], 0.48 [c]
$CuGaTe_2$	0.81	1.24 [a]
$CuInS_2$	0.5	1.53 [a], -0.14[c]
$CuInSe_2$	0.38	1.04 [a], -0.2 [c]
$CuInTe_2$	0.5	1.06 [a]

[a]experimental value in ref [16], [e] ref[20], [c]other theoretical values in ref [16],

The investigation of solid-state material systems involves studying their optical spectra, which can be characterized using techniques like photoluminescence and optical absorption. In this study, we analyze the optical properties of the aforementioned chalcopyrites using the FPLMTO "LmtART" software. To achieve a responsible description of the higher-lying unoccupied states, we employ the full potential version of the method. Optical property studies are crucial as they provide insights into both the occupied and unoccupied parts of the electronic structure, revealing the nature of the bands. Furthermore, the optical functions of ternary compounds exhibit similarities with their binary analogs [13].

The optical properties of these materials are described using the complex dielectric function $\varepsilon(\omega) = \varepsilon1(\omega) + \varepsilon2(\omega)$, where $\varepsilon1$ and $\varepsilon2$ are the real and imaginary parts of the dielectric function, respectively. The real part, $\varepsilon1(\omega)$, can be obtained from the imaginary part, $\varepsilon2(\omega)$, using the Kramers-Kronig relation. For the chalcopyrites under study, the dielectric function data are calculated for both perpendicular ($E\perp c$-axis) and parallel ($E\parallel c$-axis) polarizations, denoted as $\varepsilon2xy(\omega)$ and $\varepsilon2z(\omega)$ respectively. Figures (15-20) present the real and imaginary parts of the optical spectra for $CuGaX_2$ and $CuInX_2$ (X = S, Se, Te) chalcopyrite semiconductors. These analyses shed light on the optical characteristics of these compounds and are essential in understanding their behavior in various applications.

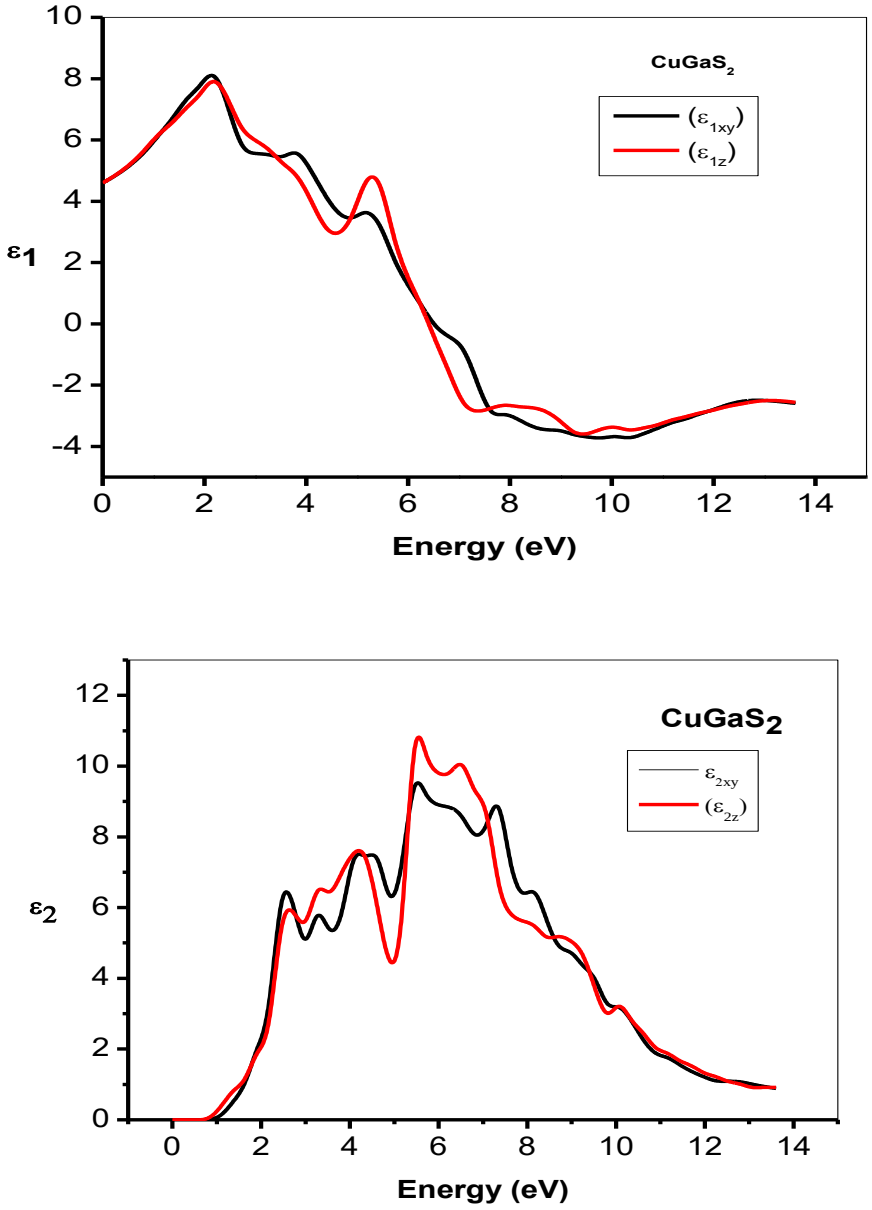

Fig: 15. The ordinary and extraordinary ray for real and imaginary parts of $CuGaS_2$

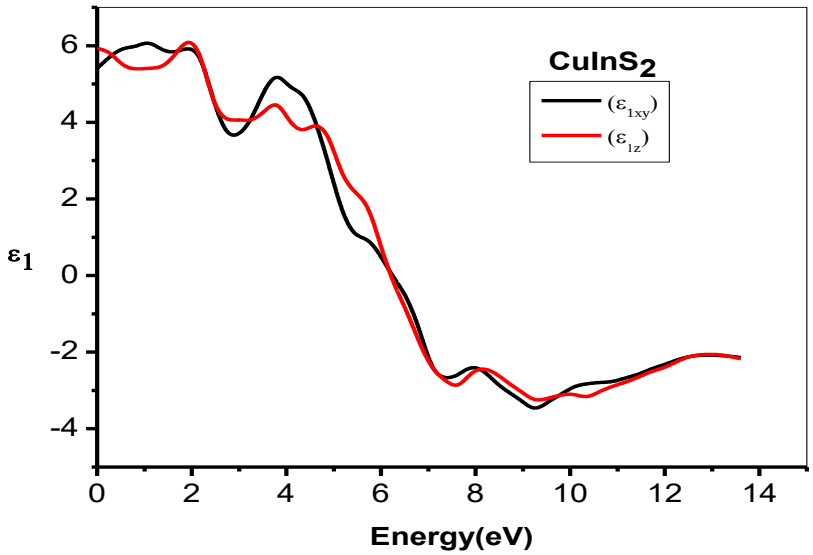

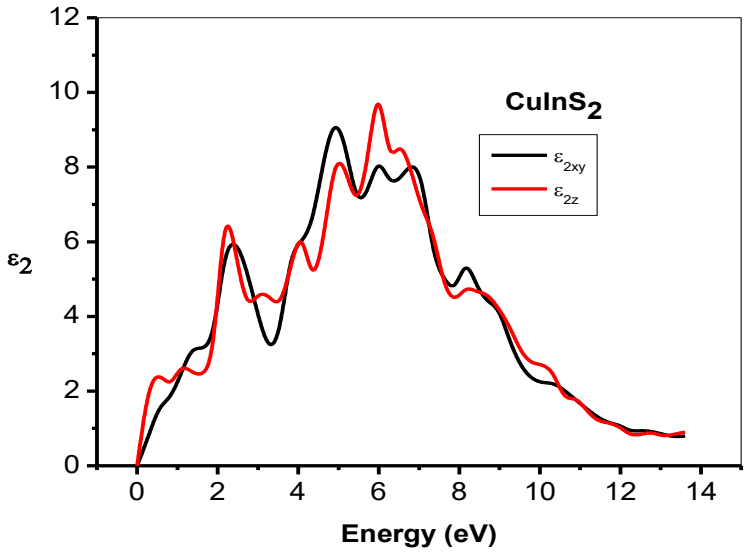

Fig: 16. The ordinary and extraordinary of the real and imaginary parts of $CuInS_2$

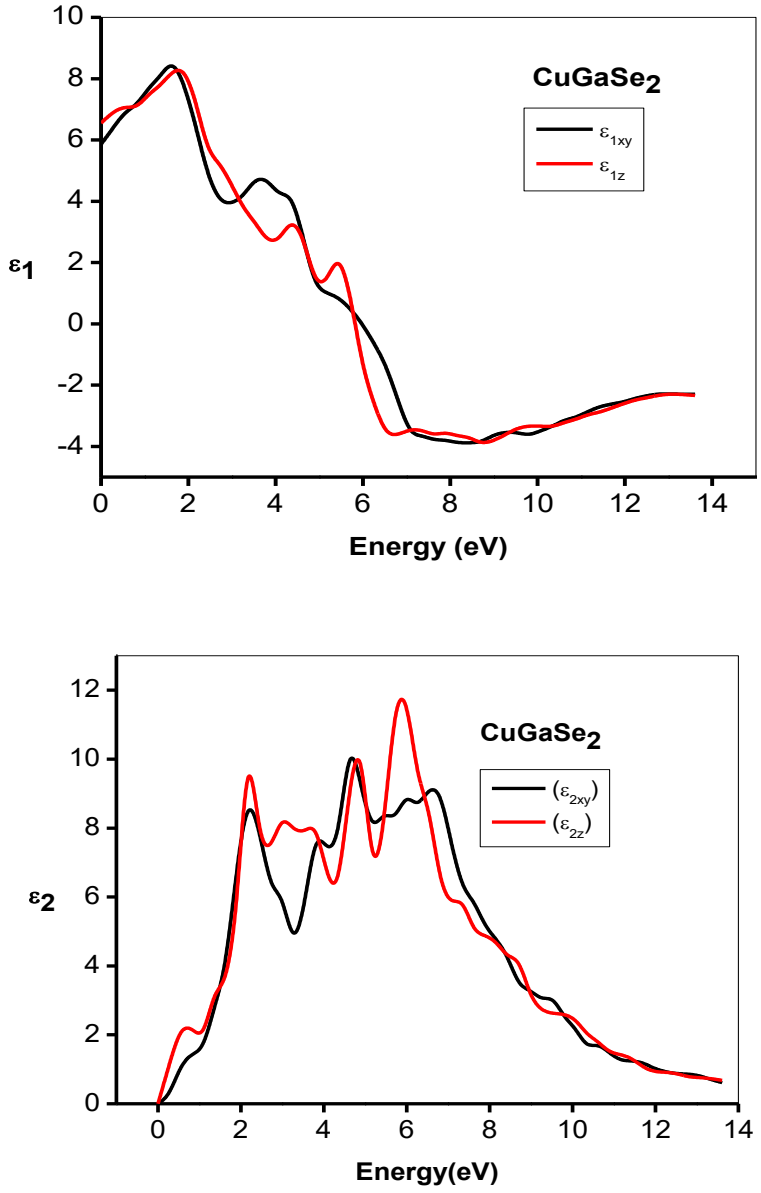

Fig: 17. The ordinary and extraordinary of the real and imaginary parts of $CuGaSe_2$

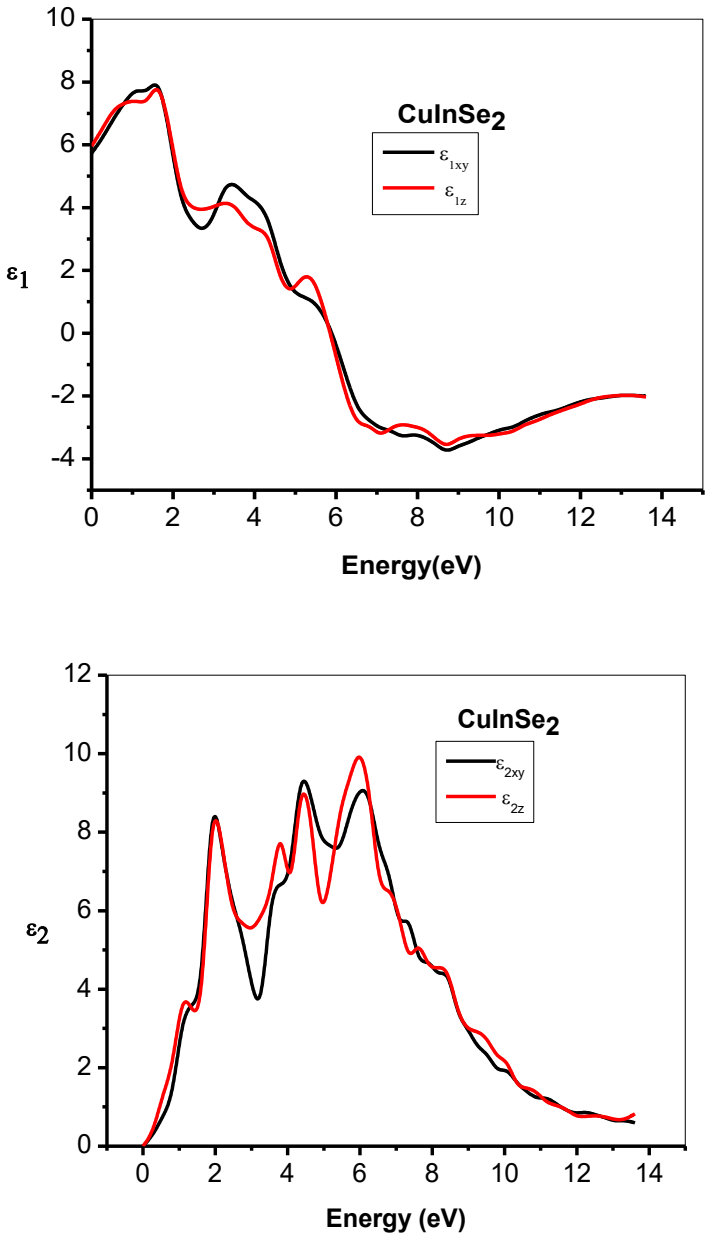

Fig: 18. The ordinary and extraordinary of the real and imaginary parts of $CuInSe_2$

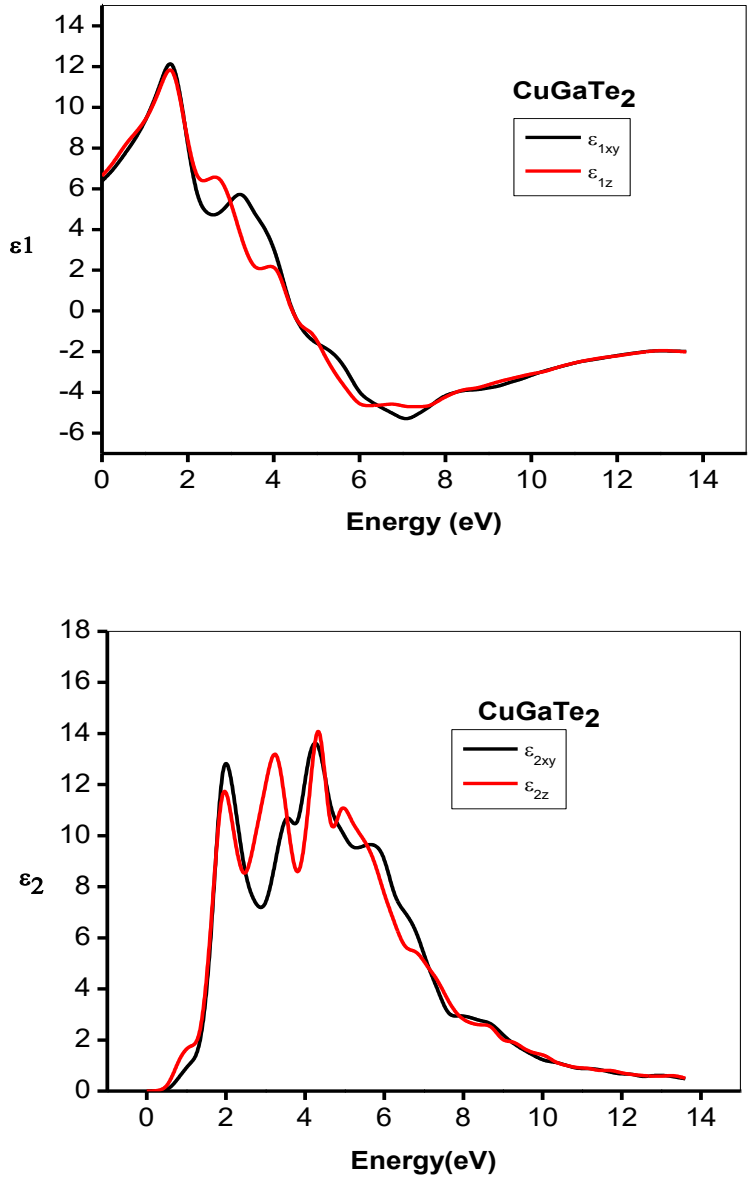

Fig: 19. The ordinary and extraordinary ray for the real and imaginary parts of $CuGaTe_2$

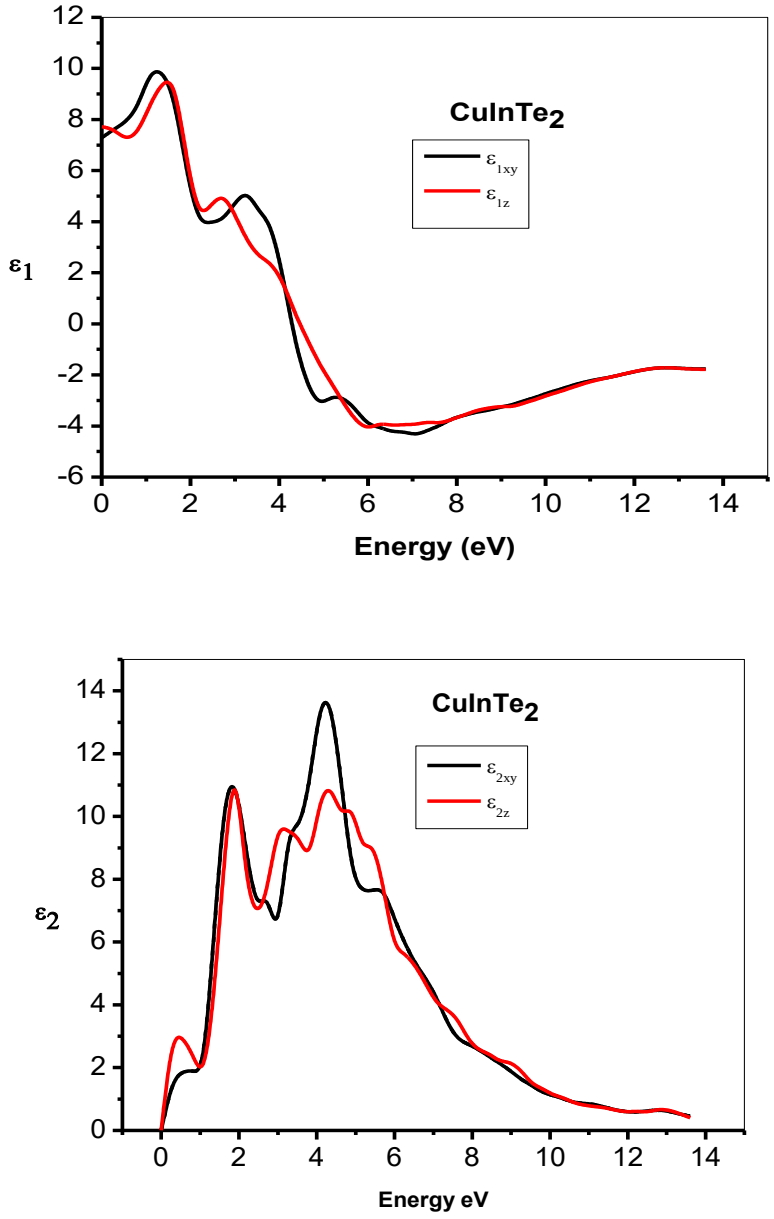

Fig: 20. The ordinary and extraordinary ray for the real and imaginary parts of $CuInTe_2$

The imaginary part curves of optical properties for $CuGaS_2$, $CuInS_2$, $CuGaSe_2$, $CuInSe_2$, $CuGaTe_2$, and $CuInTe_2$ chalcopyrite compounds show similar general shapes. Specifically, $CuGaS_2$ and $CuInS_2$ curves are nearly identical, while $CuGaSe_2$ and $CuInSe_2$ curves closely resemble those of $CuGaS_2$ compounds. Similarly, $CuGaTe_2$ and $CuInTe_2$ compounds exhibit optical property curves resembling those of $CuMS_2$ and $CuMSe_2$ compounds, respectively. This

similarity in curves is attributed to the similarities in their band structures. The prominent energy peaks observed in the imaginary part curves arise from transitions occurring at specific points in the Brillouin zone, namely Γ, N, and T points, for the compounds. These peaks can be categorized into three groups based on the points of transition: the first group corresponds to transitions at Γ point, the second group involves transitions at both Γ and N points, and the third group includes transitions at Γ, T, and N points. Table 3-9 provides the detailed values of the prominent energy peaks for ordinary and extraordinary polarizations, along with available experimental data [13].

For each of the chalcopyrite compounds, the main peak of the imaginary part curve is determined. For $CuGaS_2$, the main peak is at 5.54 eV, arising from transitions at T and N points. Similarly, the main peak values for other compounds are as follows: 5.86 eV for $CuGaSe_2$ (from transition at Γ point), 4.32 eV for $CuGaTe_2$ (from transitions at Γ and N points), 6.00 eV for $CuInS_2$ (from transition at Γ point), 5.97 eV for $CuInSe_2$ (from transitions at Γ and N points), and 4.23 eV for $CuInTe_2$ (from transitions at Γ and T points). The determination of these main peak values provides valuable insights into the optical properties and electronic transitions occurring in each chalcopyrite compound.

An important and measurable quantity in the study of these chalcopyrite compounds is the zero frequency limit of the electronic part of the static dielectric constant, denoted as ε (0). This quantity strongly depends on the bandgap of the materials and can be related to the refractive index measured at a frequency above the lattice vibrational frequencies. In Table 10, we present the calculated values of the static dielectric constant ε1 (0) and the refractive index n (0) for these chalcopyrite semiconductors. It is worth noting that the calculated values for ε1 (0) and n (0) are found to be lower than the available experimental data [19, 20]. Additionally, the table includes the calculated values for ε1⊥ (0) and ε1 וו (0), which represent the ordinary and extraordinary components of the dielectric constant, respectively.

Furthermore, the degree of anisotropy Δε for the chalcopyrite compounds is also computed and provided in the table. Notably, the values of Δε are relatively small and positive for all the compounds, indicating a limited anisotropy in their optical properties. The assessment of these static dielectric constants and refractive indices offers valuable insights into the electronic characteristics and optical behavior of the chalcopyrite semiconductors under consideration.

Table: 4 represent the prominent energy peaks of $CuGaS_2$

Main energy peak values in the optical curve (eV)		Major contributed transition	
E ⊥ c	**E ∥ c**	**Transition**	**Energy (eV)**
2.55	2.64 (2.62)[e]	$\Gamma_{5v}^{2} \rightarrow \Gamma_{1c}$	2.656
		$\Gamma_{4v}^{1} \rightarrow \Gamma_{3c}$	2.50
3.30 (3.5)[a]	3.36(3.72) [a]	$T_{3v} + T_{4v} \rightarrow T_{1c} + T_{2c}$	3.12
		$\Gamma_{4v}^{1} \rightarrow \Gamma_{2c}$	3.12
		$N_{1v}^{2} \rightarrow N_{1c}^{1}$	3.12
4.20 (4.20) [a], 4.48 (4.53) [a]	4.23(4.15) [a]	$T_{3v} + T_{4v} \rightarrow T_{5c}^{1}$	4.22
		$\Gamma_{5v}^{2} \rightarrow \Gamma_{3c}$	4.53
5.54	5.57	$N_{1v}^{2} \rightarrow N_{1c}^{2}$	5.31
		$N_{1v}^{2} \rightarrow N_{1c}^{1}$	5.62
6.25	6.47	$T_{5v} \rightarrow T_{1c} + T_{2c}$	6.09
		$\Gamma_{4v}^{1} \rightarrow \Gamma_{1c}$	6.25
7.28		$\Gamma_{3v} \rightarrow \Gamma_{2c}$	7.19
		$\Gamma_{4v}^{1} \rightarrow \Gamma_{3c}$	7.5
		$N_{1v}^{2} \rightarrow N_{1c}^{2}$	7.5
8.09		$\Gamma_{4v}^{1} \rightarrow \Gamma_{2c}$	8.13

[a] ref [13], [b] ref[20]

Table: 5 represent the main energy peaks of $CuGaSe_2$

Main energy peak values in the optical curve (eV)		Major contributed transition	
E ⊥ c	**E ∥ c**	**Transition**	**Energy (eV)**
2.21(2.8) [a]	2.18	$\Gamma_{5v}^{2} \rightarrow \Gamma_{1c}$	2.14
		$\Gamma_{5v}^{1} \rightarrow \Gamma_{2c}$	2.5
	3.06(3.127) [a] (3.08[b])	$T_{1v} + T_{2v} \rightarrow T_{1c} + T_{2c}$	2.97
3.87(3.35) [a],	3.70	$\Gamma_{3v} \rightarrow \Gamma_{1c}$	3.75
		$\Gamma_{5v}^{1} \rightarrow \Gamma_{5c}$	3.91
		$\Gamma_{4v}^{1} \rightarrow \Gamma_{5c}$	3.91
		$T_{2v} + T_{4v} \rightarrow T_{5c}^{1}$	4.06
4.69(4.89) [a]	4.81	$\Gamma_{5v}^{2} \rightarrow \Gamma_{5c}$	4.69
		$\Gamma_{4v}^{1} \rightarrow \Gamma_{1c}$	4.84
		$N_{1v}^{2} \rightarrow N_{1c}^{1}$	4.84
		$T_{2v} + T_{4v} \rightarrow T_{5c}^{2}$	4.92
5.45		$N_{1v}^{2} \rightarrow N_{1c}^{2}$	5.31
		$\Gamma_{4v}^{2} \rightarrow \Gamma_{5c}$	5.47
6.03	5.86	$\Gamma_{5v}^{2} \rightarrow \Gamma_{5c}$	6.09
6.61		$T_{4v} + T_{5v} \rightarrow T_{1c} + T_{2c}$	6.56
		$\Gamma_{4v}^{2} \rightarrow \Gamma_{1c}$	
		$\Gamma_{4v}^{1} \rightarrow \Gamma_{3c}$	6.56
	7.26	$N_{1v}^{2} \rightarrow N_{1c}^{3}$	6.72
		$T_{5v} \rightarrow T_{5c}^{2}$	7.19
		$\Gamma_{4v}^{1} \rightarrow \Gamma_{2c}$	7.266
		$N_{1v}^{2} \rightarrow N_{1c}^{2}$	7.344
			7.334

[a]ref [13]

Table: 6 represent the prominent energy peaks of $CuGaTe_2$

Main energy peak values in the optical curve (eV)		Major contributed transition	
E ⊥ c	**E ∥ c**	**Transition**	**Energy (eV)**
	1.03	$N_{1v}^{1} \rightarrow N_{1c}^{1}$	1.56
1.99	1.96	$\Gamma_{4v}^{1} \rightarrow \Gamma_{3c}$	1.87
		$\Gamma_{5v}^{1} \rightarrow \Gamma_{3c}$	1.87
		$N_{1v}^{2} \rightarrow N_{1c}^{1}$	2.19
3.54	3.23	$\Gamma_{5v}^{2} \rightarrow \Gamma_{1c}$	2.97
		$\Gamma_{4v}^{2} \rightarrow \Gamma_{3c}$	3.75
4.26	4.32	$\Gamma_{3v} \rightarrow \Gamma_{1c}$	4.22
		$T_{5v} \rightarrow T_{1c} + T_{2c}$	4.22
		$N_{1v}^{2} \rightarrow N_{1c}^{1}$	4.37
		$\Gamma_{5v}^{2} \rightarrow \Gamma_{3c}$	4.37
		$\Gamma_{5v}^{2} \rightarrow \Gamma_{2c}$	4.37
	4.97	$T_{2v} + T_{4v} \rightarrow T_{5c}^{2}$	4.84
		$T_{1v} + T_{2v} \rightarrow T_{5c}^{1}$	5.0
		$N_{1v}^{1} \rightarrow N_{1c}^{3}$	5.0
5.75		$T_{4v} + T_{5v} \rightarrow T_{1c} + T_{2c}$	5.62
		$\Gamma_{4v}^{2} \rightarrow \Gamma_{5c}$	5.78
		$\Gamma_{3v} \rightarrow \Gamma_{3c}$	5.62
		$\Gamma_{3v} \rightarrow \Gamma_{2c}$	5.62
		$N_{1v}^{2} \rightarrow N_{1c}^{3}$	5.62
		$T_{5v} \rightarrow T_{5c}^{c}$	6.72
	6.68	$\Gamma_{4v}^{1} \rightarrow \Gamma_{3c}$	6.56
		$\Gamma_{4v}^{1} \rightarrow \Gamma_{2c}$	6.56
		$\Gamma_{4v}^{2} \rightarrow \Gamma_{1c}$	6.72

Table: 7 represent the prominent energy peaks of $CuInS_2$

Main energy peak values in the optical curve (eV)		Major contributed transition	
E ⊥ c	**E ∥ c**	**Transition**	**Energy (eV)**
1.43	1.12	$\Gamma_{4v}^{2} \rightarrow \Gamma_{1c}$	1.25
2.36	2.27	$\Gamma_{5v}^{2} \rightarrow \Gamma_{1c}$	2.03
		$T_{2v} + T_{4v} \rightarrow T_{1c} + T_{2c}$	2.19
	3.11(3.09) [a]	$N_{1v}^{2} \rightarrow N_{1c}^{1}$	2.81
		$\Gamma_{4v}^{2} \rightarrow \Gamma_{3c}$	3.12
	4.04(4.05) [a]	$T_{2v} + T_{4v} \rightarrow T_{5c}^{1}$	3.90
		$\Gamma_{5v}^{2} \rightarrow \Gamma_{3c}$	3.91
4.94 (5.05) [a]	5.04(5.04) [a]	$T_{1v} + T_{2v} \rightarrow T_{5c}^{2}$	5.0
		$\Gamma_{4v}^{2} \rightarrow \Gamma_{5c}$	5.16
6.03	6.0	$\Gamma_{5v}^{2} \rightarrow \Gamma_{5c}$	5.94
6.84	6.53	$\Gamma_{3v} \rightarrow \Gamma_{3c}$	6.56
		$N_{1v}^{2} \rightarrow N_{1c}^{3}$	6.56
		$N_{1v}^{4} \rightarrow N_{1c}^{1}$	6.88
8.18	8.21	$N_{1v}^{3} \rightarrow N_{1c}^{1}$	8.12

[a]ref[13]

Table: 8 represent the prominent energy peaks of $CuInSe_2$

Main energy peak values in the optical curve (eV)		Major contributed transition	
E ⊥ c	**E ∥ c**	**E ⊥ c**	**E ∥ c**
1.99	1.99	$\Gamma_{5v}^{2} \rightarrow \Gamma_{1c}$	1.87
		$\Gamma_{4v}^{1} \rightarrow \Gamma_{3c}$	1.87
3.70(3.72) [a]	3.79	$N_{1v}^{1} \rightarrow N_{1c}^{1}$	3.75
		$\Gamma_{5v}^{2} \rightarrow \Gamma_{3c}$	3.75
4.45(4.4) [a]	4.45	$\Gamma_{3v} \rightarrow \Gamma_{1c}$	4.37
		$\Gamma_{4v}^{1} \rightarrow \Gamma_{5c}$	4.37
		$N_{1v}^{2} \rightarrow N_{1c}^{1}$	4.37
6.09	5.97	$\Gamma_{4v}^{2} \rightarrow \Gamma_{1c}$	5.94
		$N_{1v}^{2} \rightarrow N_{1c}^{2}$	5.94
		$N_{1v}^{1} \rightarrow N_{1c}^{3}$	5.93
	6.87	$\Gamma_{2v} \rightarrow \Gamma_{1c}$	6.72
		$\Gamma_{4v}^{1} \rightarrow \Gamma_{3c}$	6.87
		$T_{3v} + T_{4v} \rightarrow T_{5c}^{1}$	6.87
7.28		$T_{5v} \rightarrow T_{5c}^{2}$	
		$\Gamma_{4v}^{1} \rightarrow \Gamma_{2c}$	7.19
		$T_{3v} + T_{4v} \rightarrow T_{5c}^{2}$	7.19
7.87	7.62	$\Gamma_{4v}^{2} \rightarrow \Gamma_{3c}$	7.66
		$N_{1v}^{4} \rightarrow N_{1c}^{1}$	7.81
		$N_{1v}^{3} \rightarrow N_{1c}^{2}$	7.81
		$T_{5v}^{2} \rightarrow T_{1c} + T_{2c}$	7.81
8.37	8.31	$\Gamma_{4v}^{2} \rightarrow \Gamma_{2c}$	8.12
			8.12

[a]ref[13]

Table: 9 represent the prominent energy peaks of $CuInTe_2$

Main energy peak values in the optical curve (eV)		Major contributed transition	
E ⊥ c	**E ∥ c**	**E ⊥ c**	**E ∥ c**
1.80	1.895	$\Gamma^1_{5v} \rightarrow \Gamma_{3c}$	1.87
		$\Gamma^1_{4v} \rightarrow \Gamma_{3c}$	1.88
		$N^1_{1v} \rightarrow N^1_{1c}$	1.87
2.64		$T_{2v} + T_{4v} \rightarrow T_{1c} + T_{2c}$	2.5
		$\Gamma^2_{5v} \rightarrow \Gamma_{1c}$	2.5
		$N^2_{1v} \rightarrow N^1_{1c}$	2.5
	3.14	$T_{1v} + T_{2v} \rightarrow T_{1c} + T_{2c}$	3.12
4.23			
	4.29	$T_{2v} + T_{4v} \rightarrow T^2_{5c}$	4.22
		$\Gamma^2_{5v} \rightarrow \Gamma_{3c}$	4.38
5.51	4.82	$T_{1v} + T_{2v} \rightarrow T^2_{5c}$	4.84
		$T_{3v} + T_{4v} \rightarrow T^1_{5c}$	
	5.35	$T_{4v} + T_{5v} \rightarrow T_{1c} + T_{2c}$	5.30
		$\Gamma_{3v} \rightarrow \Gamma_{3c}$	5.31
		$N^4_{1v} \rightarrow N^1_{1c}$	5.31
		$N^2_{1v} \rightarrow N^3_{1c}$	5.31
	7.47	$T^2_{5v} \rightarrow T_{1c} + T_{2c}$	5.62
		$N^4_{1v} \rightarrow N^2_{1c}$	7.34
			7.34

Table: 10. The estimated static dielectric function and refractive index for the chalcopyrites

	$\varepsilon_1(0)$	$\varepsilon_{1\perp}(0)$	$\varepsilon_{1\parallel}(0)$	$\Delta\varepsilon$	n(0)
$CuGaS_2$	4.59(6.88[a])	4.59	4.59	0.0004	2.14 (2.62[a])
$CuGaSe_2$	6.08	5.85	6.54	0.114	2.46
$CuGaTe_2$	6.45	6.37	6.62	0.038	2.54
$CuInS_2$	5.58	5.40	5.93	0.094	2.36
$CuInSe_2$	5.80	5.72	5.94	0.039	2.41
$CuInTe_2$	7.43	7.28	7.72	0.060	2.73

[a]ref[19]

4. Conclusion

This paper investigates structural phase transitions, electronic, optical, and thermodynamic properties of $CuGaX_2$ and $CuInX_2$chalcopyrites. The TB-LMTO method is employed to study electronic and structural phase transitions, obtaining equilibrium lattice constants and bandgaps for the compounds. Under high pressure, all compounds undergo a structural change from BCT to FCC phase. The BCT phase is found to be energetically more favorable than the intermediate (d-SC) phase predicted for $CuGaTe_2$ and $CuInTe_2$. The lattice parameter increases from S to Te for both BCT and FCC phases, in agreement with experimental and theoretical values. The bulk modulus decreases from S to Te in both phases. Transition pressure and volume are calculated from fitted total energy and pressure versus relative volume graphs.Band structures reveal a direct bandgap for the BCT phase, while the FCC phase shows a metallic nature, confirming the transition from semiconductor to metal under pressure.Optical property studies using FP-LMTO 'LmtART' method focus on the occupied and unoccupied states of the electronic structure. Real and imaginary parts of the compounds are plotted, and primary energy peaks are calculated. Intraband transitions corresponding to these peaks are computed using band structure calculations. Refractive indices are also derived from the obtained real and imaginary parts of the chalcopyrites.

Acknowledgments

The authors express sincere gratitude to Professor O. K. Andersen and Professor O. Jepsen from Max Planck Institute, Stuttgart, Germany, for generously providing the TB-LMTO code.

Additionally, the authors are thankful to Professor S. Y. Savrasov from New Jersey Institute of Technology, New York, USA, for supplying the FP-LMTO code. Special thanks are extended to the CSIR for their valuable financial support that enabled the successful completion of this work.

Reference

[1] J. L. Shay and J. H. Wernick, Ternary Chalcopyrite Semiconductors: Growth, Electronic Properties, and Applications (Pergamon, Oxford, 1975).

[2] J. E. Jaffe and Alex Zunger, Phys. Rev. B 28, 5822 (1983).

[3] W. Shockley, H.J. Queisser, J. Appl. Phys. 32, 510 (1961).

[4] S. Shirakata, S. Chichibu, S. Isomura, Jpn. J. Appl. Phys. 36, 7160 (1997).

[5] T. Maeda, T. Takeichi, Phys. Stat. Sol. (a) 203, 2634 (2006).

[6] B. Xu, X. Li, Z. Qin, Physica B 406, 946 (2011).

[7] I. Aguilera, J. Vidal, Phys. Rev. B 84, 085145 (2011).

[8] Li Xue, Yi-Ming Ren, Jun-Rong He, and Si-Liu Xu, Chin. Phys. B Vol. 26, No. 6, 067103 (2017).

[9] Hao Yu, Ge Huang, Qing Peng, Liu-Cheng Chen, Hong-Jie Pang, Xiao-Ying Qin, Peng-Fei Qiu, Xun Shi, Li-Dong Chen, Xiao-Jia Chen, Journal of Alloys and Compounds 822, 153610 (2020).

[10] Werner A, Hocheimer D H and Jayaraman A, Phys. Rev. B 23, 3836 (1981).

[11] Tinoco T, Polian A, Gomez D and Itie J.P, Phys. Stat. Sol. (b) 198, 433 (1996).

[12] Gonzalez J and Rincon C, J. Phys. Chem. Solids 51, 1093 (1990).

[13] Alonso M. I, Pascual J, Garriga M, Kilkuno Y, Yamamoto N and Wakita K, J. Appl. Phys. 88, 1923 (2000).

[14] Mori Y, Ikai T and Takarabe K, Phys. Stat. Sol. (b) 235, 317 (2003).

[15] Jaffe J. E. and Zunger A., Phys. Rev. B 27, 5176 (1983).

[16] Jaffe J. E. and Zunger A., Phys. Rev. B 28, 5822 (1983).

[17] Jaffe J. E. and Zunger A., Phys. Rev. B 29, 1882 (1984).

[18] Lazewski J, Jochym P.T and Parlinski K, J. Chem. Phys. 117, 2726 (2002).

[19] Belhadj M, Tadjaer A, Abbar B, Bousahala Z, Bouhats B and Aourag H, Phys. Stat. Sol. (b) 241, 2516 (2004).

[20] S. Laksari, A. Chahed, N. Abbouni, O. Benhelal, B. Abbar, Computational Materials Science, Volume 38, Issue 1, November 2006, Pages 223-230

[21] Jayalakshmi V, Davapriya S, Murugan R, Palanivel B, J. Phys. Chem. Solids 67, 669 (2006).

[22] Anderson O. K., Jepson O, Phys. Rev. Lett. 53, 2871 (1984).

[23] Anderson O. K., Phys. Rev. B 12, 3060 (1975).

[24] Skriver H. L., The LMTO Method, Springer, Berlin, 1984.

[25] Savrasov S. Y. Phys. Rev. B 54, 16470 (1996).

[26] von Barth U, Hedin L, J. Phys. 5, 1629 (1972).

[27] H. Neumann, Phys. Stat.sol. (a) 96, K121 (1986).

[28] H. Neumann, Crystal Res. Technol. 18, 665 (1983).